ORIGINAL RESEARCH

Hollow Mesoporous Molybdenum Single-Atom Nanozyme-Based Reactor for Enhanced Cascade Catalytic Antibacterial Therapy

Zhijun Zhang [1,2], Tiehong Yang[2], Jingwei Wang[2], Zhe Yu[2], Youbei Qiao [2], Chaoli Wang[2], Zhenggang Yue[1], Hong Wu [2]

[1]School of Pharmacy, Shaanxi University of Chinese Medicine, Xi'an, People's Republic of China; [2]Department of Medicine Chemistry and Pharmaceutical Analysis, School of Pharmacy, Air Force Medical University, Xi'an, People's Republic of China

Correspondence: Hong Wu, Department of Medicine Chemistry and Pharmaceutical Analysis, School of Pharmacy, Air Force Medical University, Xi'an, People's Republic of China, Tel/Fax +86 29 84776823, Email wuhong@fmmu.edu.cn; Zhenggang Yue, School of Pharmacy, Shaanxi University of Chinese Medicine, Xi'an, People's Republic of China, Tel +86 18092086211, Email liuxingjian1981@163.com

Purpose: The remarkable peroxidase-like activity of single-atom nanozymes (SAzymes) allows them to catalyze the conversion of H_2O_2 to •OH, rendering them highly promising for antibacterial applications. However, their practical in vivo application is hindered by the near-neutral pH and insufficient H_2O_2 levels present in physiological systems. This study was aimed at developing a SAzyme-based nanoreactor and investigating its in vivo antibacterial activity.

Methods: We developed a hollow mesoporous molybdenum single-atom nanozyme (HMMo-SAzyme) using a controlled chemical etching approach and pyrolysis strategy. The HMMo-SAzyme not only exhibited excellent catalytic activity but also served as an effective nanocarrier. By loading glucose oxidase (GOx) with HMMo-SAzyme and encapsulating it with hyaluronic acid (HA), a nanoreactor (HMMo/GOx@HA) was constructed as glucose-triggered cascade catalyst for combating bacterial infection in vivo.

Results: Hyaluronidase (HAase) at the site of infection degraded HA, allowing GOx to convert glucose into gluconic acid and H_2O_2. An acid environment significantly enhanced the catalytic activity of HMMo-SAzyme to promote the further catalytic conversion of H_2O_2 to •OH for bacterial elimination. In vitro and in vivo experiments demonstrated that the nanoreactor had excellent antibacterial activity and negligible biological toxicity.

Conclusion: This study represents a significant advancement in developing a cascade catalytic system with high efficiency based on hollow mesoporous SAzyme, promising the advancement of biological applications of SAzyme.

Keywords: nanozyme, nanocarrier, glucose oxidase, reactive oxygen species, bacterial infection

Introduction

Bacterial infections pose significant health threats to humans.[1,2] The widespread use of antibiotics in clinical practice has led to the rise and rapid spread of antibiotic-resistant bacteria, which has caused a crisis of antibiotic use and seriously threatens human health.[3,4] Thus, the development of novel antibacterial agents or strategies is crucial.

Nanozymes are defined as nanomaterials that catalyze the conversion of enzyme substrates to products and follow enzymatic kinetics.[5] In recent years, nanozymes, especially single-atom nanozymes (SAzymes), have been widely investigated in the biomedical field owing to their excellent enzyme-like activity or photodynamic or photothermal properties.[6–9] Among them, SAzymes with peroxidase-like activity have garnered considerable attention in the field of antibacterial research owing to their ability to effectively catalyze the generation of •OH from H_2O_2, causing irreversible oxidative damage to bacteria without promoting bacterial drug resistance.[10–13] However, the enzyme-like activity of SAzymes is optimal under strongly acidic conditions with pH 3–4.[14,15] Nonetheless, bacterial infection sites typically exhibit weakly acidic or nearly neutral pH.[16,17] Moreover, higher H_2O_2 concentrations are generally required to generate sufficient •OH for effective antibacterial applications owing to in vivo depletion of free radicals by glutathione.[18–20] High

Graphical Abstract
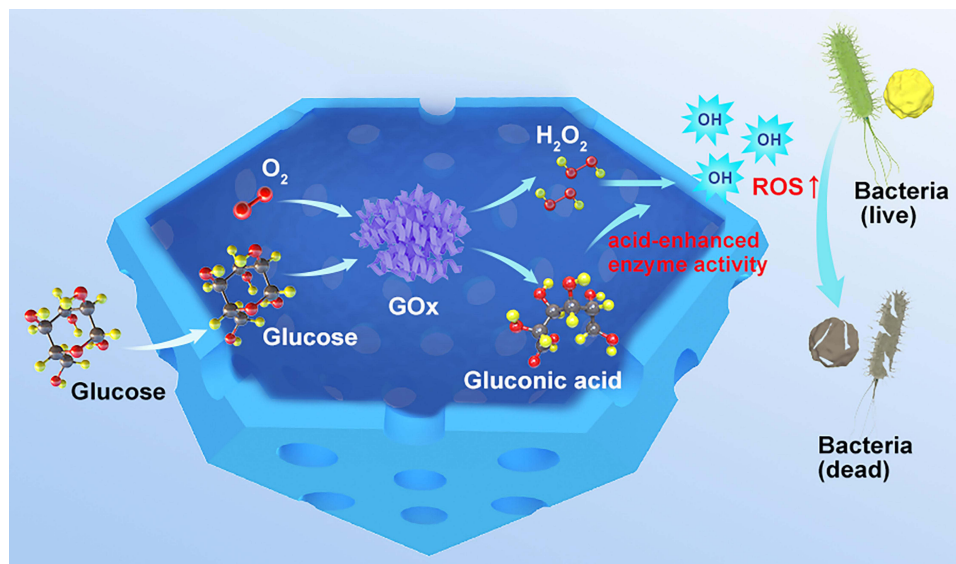
H_2O_2 concentrations can lead to immunogenicity, inflammation, and tissue damage,[21,22] severely limiting the in vivo antibacterial application of SAzymes.

Glucose oxidase (GOx) is a commonly used and safe natural enzyme that continuously converts glucose into gluconic acid and H_2O_2.[23–26] The use of SAzyme and GOx together is expected to solve the H_2O_2 and pH constraints of SAzyme in antibacterial applications in vivo. However, most of the reported SAzymes are solid structures lacking a hollow cavity, which hinders effective loading of GOx.

Among various nanomaterials, hollow mesoporous nanomaterials have garnered considerable attention owing to their unique structure and excellent catalytic performance.[27–30] The hollow mesoporous structure offers several advantages, including a significant increase in specific surface area, exposure of more active sites, and enhanced mass transport within the material, resulting in improved catalytic activity.[31,32] More importantly, the hollow mesoporous structure enables nanomaterials to have a high load capacity, opening up the possibility for synthesizing composite antibacterial nanosystems.[33–35] Therefore, we propose the preparation of a SAzyme with a hollow mesoporous structure, which can achieve an efficient catalytic cascade reaction by loading GOx to promote the in vivo antibacterial application of SAzyme. However, such hollow mesoporous SAzymes, acting both as a nanocarrier and nanozyme, for in vivo antibacterial applications have rarely been investigated.

Molybdenum is an indispensable trace element in the human body. It is widely present in a variety of molybdenum enzymes and plays an important role in maintaining the stability of various body functions.[36] In recent years, Mo-based nanozymes have gained widespread attention in the biomedical field owing to their excellent peroxidase-like activity and biosafety.[37–39] In this study, we developed a novel hollow mesoporous molybdenum single-atom nanozyme (HMMo-SAzyme) that exhibits high catalytic activity while also serving as a carrier. Building upon this foundation, we constructed a nanoreactor (HMMo/GOx@HA) capable of in vivo antibacterial activity. The nanoreactor involved encapsulating GOx with HMMo-SAzyme and further modifying it with hyaluronic acid (HA) (Scheme 1). During in vivo antibacterial activity, hyaluronidase (HAase) at the site of infection degraded the outer layer of HA, allowing GOx to continuously convert glucose into gluconic acid and H_2O_2. This approach avoids the direct use of higher concentrations of H_2O_2, thereby, minimizing potential side effects. Additionally, the generated gluconic acid lowered the local pH around the HMMo-SAzyme, further enhancing its catalytic activity and promoting •OH production. In vitro and
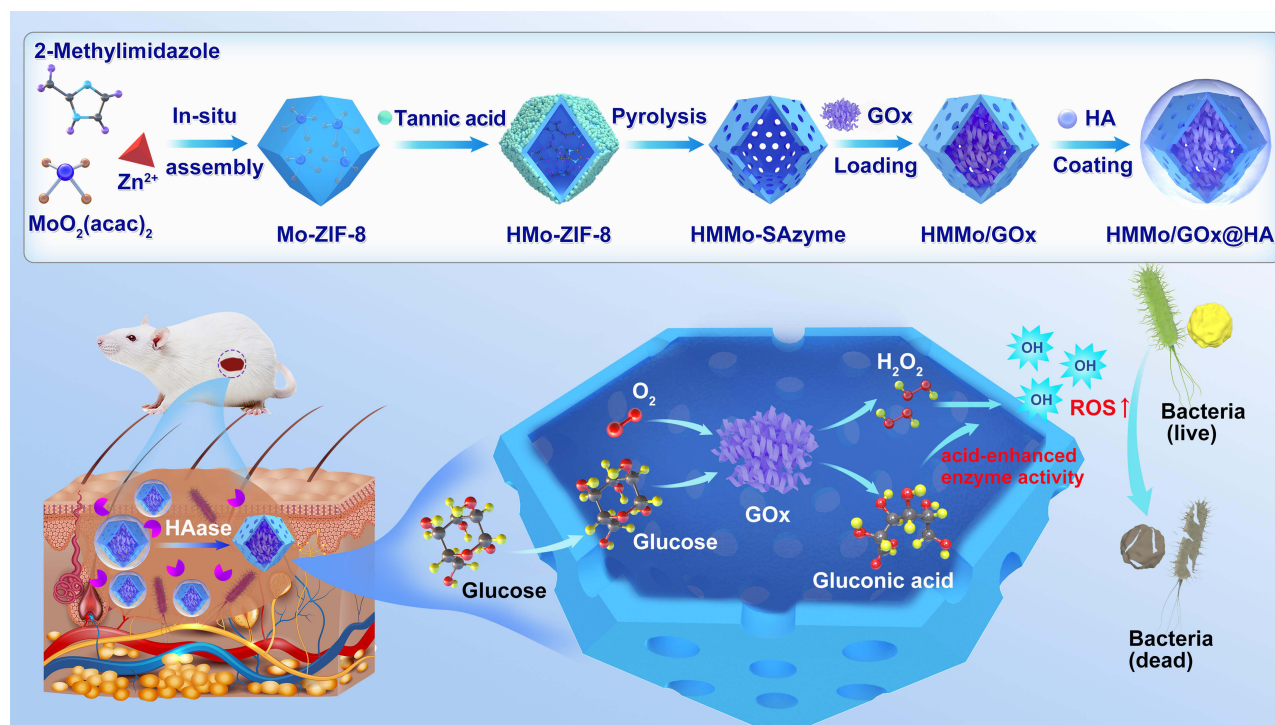
Scheme I Schematic illustration of the construction of the HMMo/GOx@HA nanoreactor and the cascade catalytic antibacterial therapy.

in vivo experiments validated the outstanding antibacterial activity of the HMMo/GOx@HA nanoreactor based on the cascade catalytic reaction, demonstrating minimal biological toxicity, rendering it a safe and efficient antibacterial agent.

Materials and Methods

Materials

2-Methylimidazole ($C_4H_6N_2$, 98.0%), molybdenyl acetylacetonate ($MoO_2(acac)_2$), tannic acid, 3,3',5,5'-tetramethylbenzidine (TMB, >99%) and hyaluronidase (HAase) were purchased from Aladdin Biochem Technology Co., Ltd (Shanghai, China). Zinc(II) nitrate hexahydrate ($Zn(NO_3)_2 \cdot 6H_2O$, 99.0%), methanol (CH_3OH, AR), hydrogen peroxide (H_2O_2, 30% aqueous solution), terephthalic acid (TA, 99%), sodium hydroxide (NaOH) and hydrochloric acid (HCl) were bought from Sinopharm Chemical Reagent Co., Ltd (Shanghai, China). Glucose oxidase (GOx) was ordered from Sigma-Aldrich (St. Louis, MO, USA). Hyaluronic acid (HA), glucose and methyl red (95%) were obtained from Macklin Biochemical Co., Ltd (Shanghai, China). Enhanced BCA protein assay kit and reactive oxygen species assay kit were bought from Beyotime Biotechnology Inc. (Shanghai, China). LB broth agar and LB broth were bought from Sangon Biotechnology Inc. (Shanghai, China). Live/dead baclight bacterial viability kits and cell counting kit-8 (CCK-8) were obtained from Thermo Fisher Scientific Inc (Waltham, MA, USA). Dulbecco's modified eagle's medium (DMEM), fetal bovine serum (FBS), phosphate buffered saline (PBS), penicillin, streptomycin and trypsin were purchased from Gibco BRL (CA, USA).

Hematoxylin-Eosin (H&E) staining kit, Masson staining kit, and Interleukin-6 antibody were purchased from Servicebio Technology Co., Ltd (Wuhan, China). Ultrapure water was used in all experiments and supplied by Milli-Q Advantage A10 (CA, USA). All reagents were purchased from commercial sources and used without any further purification.

Characterization

Scanning electron microscope (SEM, Hitachi, S4800, Japan) was used to observe the morphology of nanoparticles and bacteria. Transmission electron microscope (TEM, Hitachi, HT-7700, Japan) was used to observe the morphology and structure of samples. The high-angle annular dark-field scanning TEM (HAADF-STEM) images were collected on a high-resolution

transmission electron microscope (Thermo Scientific, Themis Z, USA). The elemental mappings were performed using a transmission electron microscope (Thermo Scientific, Talos F200X, USA). X-ray diffraction (XRD, BrukerAXS D8) was applied to measure the crystal structure. Nitrogen adsorption/desorption isotherms and pore size distributions of samples were measured by surface area and porosimetry analyzer (Micromeritics, ASAP2460, USA). The metal loadings of nanoparticles were collected by an iCAP7600 inductively coupled plasma optical emission spectroscopy (ICP-OES) instrument (Thermo Scientific, ICAP 7200, USA). The hydrodynamic size and Zeta potential were measured by Zetasizer Nano S (ZEN 3600; Malvern, England). The UV–vis absorption spectrum was detected with UV spectrophotometer (Shimadzu, UV-2600, Japan). The fluorescent spectra was measured on a fluorescence spectrophotometer (Shimadzu, RF-6000, Japan). The fluorescence images were recorded with confocal laser scanning microscope (CLSM, Nikon A1R, Japan). The H&E and Masson samples were examined under a digital microscope (IX73, OL YMPUS, Japan).

Preparation of HMMo-SAzyme and HMMo/GOx@HA Nanoreactor

2-methylimidazole (3700 mg) was dissolved in 80 mL of methanol. Zn $(NO_3)_2 \cdot 6H_2O$ (1666 mg) and $MoO_2(acac)_2$ (130 mg) were dissolved in 40 mL of methanol, then the two solutions were mixed and stirred for 12 h at room temperature. The obtained product was centrifugated at 8500 rpm, washed with methanol three times, and then freeze-drying for 12 h to obtain Mo-ZIF-8. Subsequently, 100 mg Mo-ZIF-8 was dispersing in 20 mL ultrapure water, 1.25 mL tannic acid aqueous solution (25 mg/mL) was added and stirred at room temperature for 10 min. The obtained product was centrifuged at 12,000 rpm, washed with ultrapure water three times, and then freeze-drying for 12 h to obtain HMo-ZIF-8. Finally, the HMo-ZIF-8 sample was pyrolyzed at 900 °C for 3 h under N_2 atmosphere to obtain HMMo-SAzyme.

HMMo-SAzyme (4 mL, 1 mg/mL) was mixed with GOx (4 mL, 2 mg/mL) and stirred slightly at 4 °C for 12 h. The mixture was then centrifuged to obtain HMMo/GOx, which was added to an aqueous solution of HA (4 mL, 8 mg/mL) and the mixture was gently stirred at room temperature for 6 h. The obtained product was centrifuged at 12,000 rpm and washed with ultrapure water three times to obtain HMMo/GOx@HA.

Detection of Peroxidase-Like Catalytic Activity of HMMo-SAzyme

Experiment was performed in 4 mL PBS (0.01 M, pH 3.0), including 50 μg/mL of HMMo-SAzyme, 5 mM of H_2O_2, 1 mM of TMB, and the reaction was carried out for 5 min at room temperature. The change in color of each reaction solution was observed, and the absorbance at 652 nm was measured. TA was used as a fluorescent probe to detect the production of •OH. Experiment was performed in 4 mL PBS (0.01 M, pH 3.0), and the reaction mixture contained HMMo-SAzyme (50 μg/mL), H_2O_2 (5 mM), and TA (0.5 mM). After 12 h, the fluorescence spectra of the product, 2-hydroxyterephthalic acid, was recorded.

Cascade Reaction of HMMo/GOx + Glucose

Following reaction system groups were prepared: (1) PBS, (2) glucose, (3) HMMo/GOx, (4) glucose + HMMo-SAzyme, (5) glucose + GOx, and (6) glucose + HMMo/GOx. The reactions were performed in PBS (0.5 mM, pH 7.0). Each reaction included HMMo/GOx (100 μg/mL), HMMo-SAzyme (100 μg/mL), GOx (5 μg/mL), and glucose (5 mM). The reactions were performed at 37 °C for 3 h, and the pH values were measured for each group. Subsequently, 1 mM of TMB was added to each reaction, and the absorbance of each solution was measured. Similarly, 50 mM 5.5-dimethyl-1-pyrroline N-oxide (DMPO) was added to each of the above reaction systems and the generated ROS were identified using electron spin resonance (ESR) spectroscopy.

In vitro Antibacterial Activity of HMMo/GOx@HA

Staphylococcus aureus Rosenbach (*S. aureus*, ATCC25923) and *Escherichia coli* (*E. coli*, ATCC 25922) were purchased from Fuxiang Biotechnology Co., Ltd (Shanghai, China). Single colonies of *S. aureus* and *E. coli* were transferred from solid LB agar plate to liquid LB broth. The bacteria were cultured with shaking at 37 °C for 8 h and then diluted to a concentration of 1×10^7 CFU/mL. The bacterial suspensions were treated with the following solutions: (1) PBS, (2) glucose, (3) HMMo/GOx@HA, (4) glucose + HMMo-SAzyme, (5) glucose + GOx, and (6) glucose + HMMo/GOx@HA. The bacterial suspensions were incubated at 37 °C with shaking at 180 rpm. The concentrations of glucose,

HMMo/GOx@HA, HMMo-SAzyme, and GOx were 15 mM, 100 μg/mL, 100 μg/mL and 5 μg/mL, respectively. After 5 h of incubation, the bacterial suspensions were diluted 10,000 times with LB broth. Subsequently, 100 μL of the diluted bacterial suspension was spread onto solid medium and cultured for 24 h at 37 °C. The number of colony-forming units (CFU) was counted to evaluate the antibacterial effect of the nanoreactor.

SEM Characterization of Bacterial Samples

The bacterial suspensions in the above six groups were centrifuged, washed with aseptic PBS, and fixed with 2.5% glutaraldehyde at 4 °C for 2 h. The fixed bacteria were sequentially dehydrated with 30%, 50%, 70%, 80%, 90%, 95%, and 100% ethanol. Finally, the dried bacteria were sputter-coated with gold, and observed using SEM.

Staining of Live/Dead Bacteria

The bacterial suspensions in the above six groups were centrifuged and washed. The bacteria were then stained with a fluorescent nucleic acid stain containing a mixture of propidium iodide (PI) (3 μL, 20 mM) and SYTO 9 (3 μL, 3.34 mM) for 30 min at room temperature in the dark. Finally, the stained bacteria were washed three times to remove excess dyes and imaged using CLSM.

Detection of ROS Levels in Bacteria

The bacterial suspension was treated with glucose + HMMo/GOx@HA for 3 h, and then 10 μM DCFH-DA was added. This suspension was further incubated at 37 °C in the dark for 30 min. Finally, the bacteria were washed three times, and imaged using CLSM.

Hemolysis Assay

Fresh whole blood was collected from the inner canthus vein of mice, and red blood cells were isolated from serum by centrifugation. Red blood cells were incubated with 31.25, 62.5, 125, 250, or 500 μg/mL HMMo/GOx@HA at 37 °C for 4 h. Each sample was then centrifuged and the absorbance of the supernatant at 540 nm was measured to evaluate the hemolysis rate. The hemolysis rate was calculated according to the following formula:

$$Hemolysis\ Rate(\%) = (A_M - A_S)/(A_P - A_S) \times 100\%$$

Where A_M is the absorbance of red blood cells incubated with HMMo/GOx@HA, A_S is the absorbance of red blood cells incubated with saline, and A_P is the absorbance of red blood cells incubated with ultrapure water.

In vitro Cytotoxicity Test

Human umbilical vein endothelial cells (HUVECs) were obtained from the Cell Bank of Type Culture Collection of the Chinese Academy of Sciences (Shanghai, China). The cytotoxicity of HMMo/GOx@HA was determined using the CCK-8 assay. HUVECs were seeded into a 96-well plate (5×10^3 cells/well) and cultured in a humidified 5% CO_2 incubator at 37 °C for 24 h. The HMMo/GOx@HA solutions at various concentrations were added to the 96-well plate, which were then incubated for 24 h. The cells were rinsed with PBS after the solution was removed from the wells. Finally, 10% CCK-8 was added to the wells. The absorbance at 450 nm was measured and the cell viability was determined using the following formula:

$$Cell\ Viability(\%) = (A_M - A_S)/(A_P - A_S) \times 100\%$$

Where A_M is the absorbance of cells treated with HMMo/GOx@HA, A_S is the background absorbance, and A_P is the absorbance of the well with control treatment.

In vivo Bacterial Infection Treated with the HMMo/GOx@HA Nanoreactor

Male BALB/c mice, aged 6–8 weeks, were obtained from the Experimental Animal Center of the Air Force Medical University. To establish the infected wound model, a 6 mm wound was created on the back of mice, and *S. aureus* cells (3×10^7 CFU, 50 μL) were injected into the wound. After 24 h, the mice infected with *S. aureus* were randomly divided into six groups, each consisting of five mice. The mice were treated with the following samples every 24 h for 7 days: (1)

PBS, (2) glucose, (3) HMMo/GOx@HA, (4) glucose + HMMo-SAzyme, (5) glucose + GOx, and (6) glucose + HMMo/GOx@HA. The concentrations of glucose, HMMo/GOx@HA, HMMo-SAzyme, and GOx were 15 mM, 100 μg/mL, 100 μg/mL and 5 μg/mL, respectively, and their volume were 100 μL. The wounds in each group were measured and photographed every other day to monitor the healing progress. After 7 days, the infected wound tissue of the mice was homogenized and placed in 1 mL of aseptic saline, followed by incubation at 37 °C for 24 h. The bacterial content at the infected sites was analyzed using the plate colony method. Furthermore, wound tissue from the mice was collected for H&E and Masson staining, and IL-6 immunofluorescence staining.

Statistical Analysis

SPSS 20.0 was used to analyze the data. Data are presented as mean ± SD from at least three independent experiments. The independent samples *t*-test was used to compare the group differences. *P*-values were two-tailed and a *p*-value <0.05 was considered statistically significant.

Results and Discussion
Preparation and Characterization of the HMMo/GOx@HA Nanoreactor

The process for preparation of HMMo-SAzyme is depicted in Scheme 1. Initially, MoO_2 $(acac)_2$ molecules were encapsulated within a zeolitic imidazolate framework-8 (ZIF-8) to form a molybdenum-doped zeolitic imidazolate framework (Mo-ZIF-8). The proper diameter of the $MoO_2(acac)_2$ molecule (9.06 Å) allowed it to be in situ encapsulated within ZIF-8, as it was between the size of the pores (3.4 Å) and the cavities (11.6 Å) of the host ZIF-8 structure.[40] SEM and TEM images (Figure S1) revealed a uniform rhombic dodecahedron configuration of the resulting Mo-ZIF-8, which was consistent with the previously reported structure of ZIF-8 crystals.[41] Furthermore, XRD patterns of Mo-ZIF-8 and ZIF-8 were found to be mostly identical (Figure S2), indicating that the introduction of MoO_2 $(acac)_2$ did not affect the main structure of ZIF-8.

Next, Mo-ZIF-8 was subjected to etching with tannic acid. During the etching process, some tannic acid molecules were absorbed onto the surface of Mo-ZIF-8, providing protection to its outer layer. The protons released by tannic acid were able to penetrate the inner core of Mo-ZIF-8 and subsequently etched its internal core,[42,43] resulting in the formation of a hollow molybdenum-doped zeolitic imidazolate framework (HMo-ZIF-8). As evident from the SEM and TEM images (Figure S3), HMo-ZIF-8 largely retained the morphology of Mo-ZIF-8, while an internal hollow structure appeared. The XRD patterns of HMo-ZIF-8 and ZIF-8 were found to be mostly identical (Figure S2), indicating that the etching process did not alter the original skeleton unit structure of ZIF-8.

Finally, HMo-ZIF-8 was subjected to pyrolysis at 900 °C. During this process, the $MoO_2(acac)_2$ molecules confined within the cage underwent pyrolytic conversion, transforming into Mo anchored on nitrogen-doped porous carbon (C–N) substrates.[44] The Zn atoms of the host material gradually evaporated at high pyrolysis temperature, leading to the decomposition of C–N skeletons and facilitating the formation of Mo–N bonds,[45,46] resulting in the formation of HMMo-SAzyme. SEM and TEM images (Figure 1A and B) revealed that the prepared HMMo-SAzyme retained the rhombic dodecahedron morphology of HMo-ZIF-8, exhibiting a hollow and porous structure. Nitrogen adsorption-desorption isotherms further confirmed the mesoporous framework of HMMo-SAzyme (Figure S4). The pore size, total pore volume, and specific surface area were determined to be 7.54 nm, 0.33 cm^3/g, and 346.72 m^2/g, respectively. Energy-dispersive X-ray spectroscopy (EDS) mapping demonstrated homogeneous distribution of C, N, and Mo within HMMo-SAzyme (Figure 1D). Additionally, the Mo concentration in HMMo-SAzyme was quantified to be 0.78 wt.% using ICP-OES. The XRD pattern of HMMo-SAzyme (Figure S5) displayed only two (002) and (101) diffraction peaks, characteristic of graphitic carbon, with 2θ at approximately 24° and 43°, respectively. No crystalline peaks corresponding to metallic Mo were observed, indicating the absence of large crystalline particles of Mo-containing species. Furthermore, bright dots visible in the HAADF-STEM image (Figure 1C) corresponded to isolated Mo atoms dispersed on the nitrogen-doped carbon framework owing to the higher Z-contrast of Mo atoms compared with that of N and C atoms.[47,48] These comprehensive results validated the successful preparation of the HMMo-SAzyme.

Furthermore, we loaded GOx inside the HMMo-SAzyme and coated it with HA to construct the HMMo/GOx@HA nanoreactor. Results of UV–vis spectroscopy (Figure S6) revealed cross-fused absorption peaks after GOx was loaded
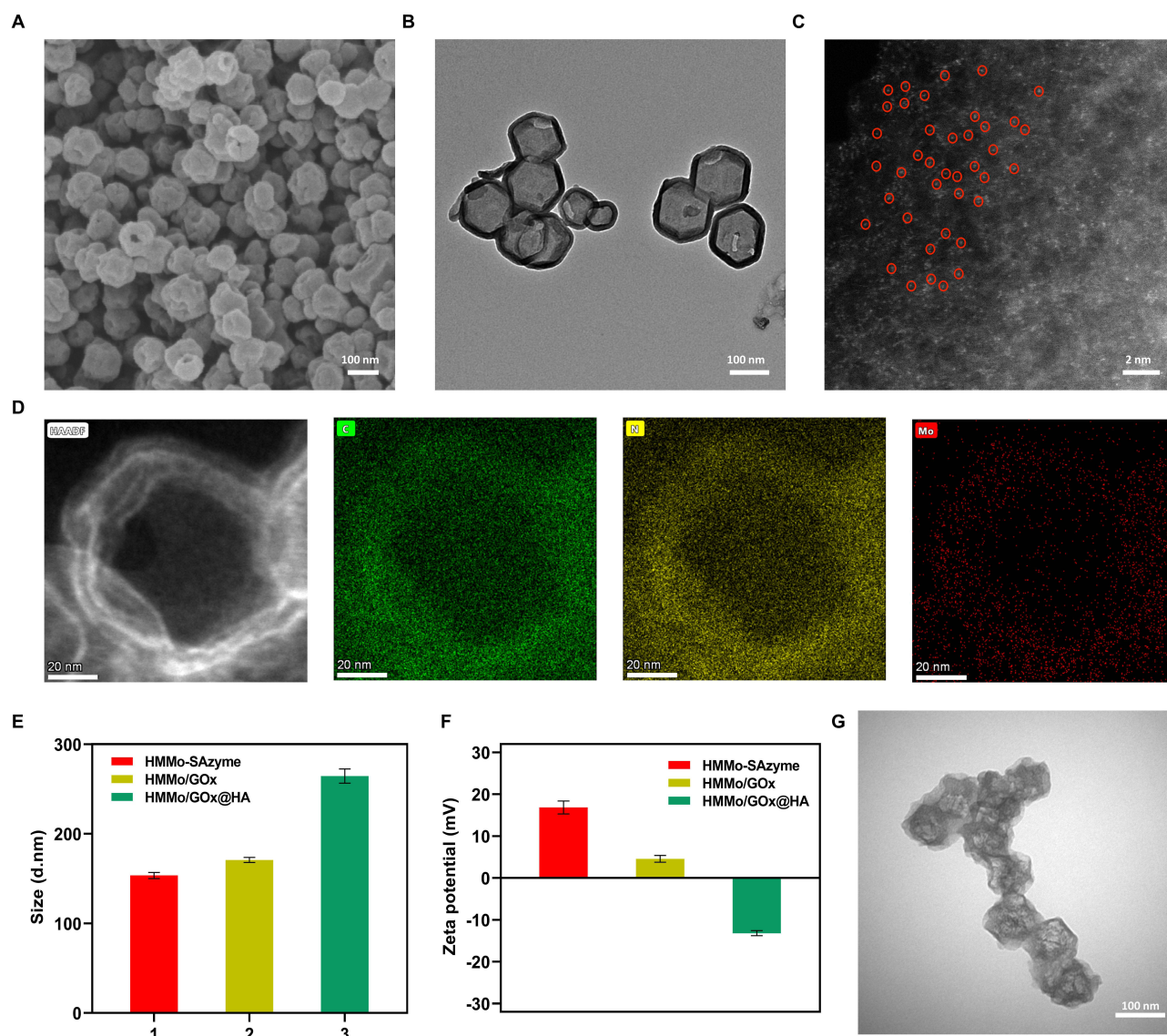
Figure 1 (**A**) SEM and (**B**) TEM images of HMMo-SAzyme. (**C**) HAADF-STEM images of HMMo-SAzyme exhibiting dispersive single Mo atoms as bright dots (indicated by red circles). (**D**) EDS mapping images of HMMo-SAzyme. (**E**) Hydrodynamic size and (**F**) zeta potential of HMMo-SAzyme, HMMo/GOx, and HMMo/GOx@HA. Data are shown as mean ± SD. (**G**) TEM images of HMMo/GOx@HA.

onto HMMo-SAzyme, indicating the successful loading of GOx. Additionally, changes in hydrodynamic size (Figure 1E) and zeta potential (Figure 1F) at each step confirmed the successful preparation of the nanoreactor. The zeta potential of HMMo-SAzyme, HMMo/GOx, and HMMo/GOx@HA was +16.85, +4.55, and −13.21 mV, respectively. These values indicated that both GOx loading and HA encapsulation were achieved through electrostatic adsorption. Notably, elemental S is an important component of GOx. EDS elemental mapping of the nanoreactor demonstrated a uniform distribution of S throughout the interior and surface of HMMo-SAzyme, providing direct evidence of successful GOx loading (Figure S7). Quantitative analysis through bicinchoninic acid (BCA) assay confirmed that the amount of GOx assembled on HMMo/GOx@HA accounted for approximately 4.87 wt.% (Figure S8). Moreover, TEM images revealed that the surface of HMMo/GOx was coated with a sticky HA layer (Figure 1G). Collectively, these results provide strong evidence for the successful construction of the HMMo/GOx@HA nanoreactor.

Catalytic Activity of the HMMo/GOx@HA Nanoreactor

The peroxidase-like activity of HMMo-SAzyme was detected using TMB as a peroxidase substrate. Figures 2A and S9 demonstrated that, in the presence of H_2O_2, HMMo-SAzyme efficiently catalyzed the oxidation of TMB, resulting in the formation of a dark blue product, oxTMB, with a characteristic absorption peak at 652 nm. Conversely, when either HMMo-SAzyme or H_2O_2 was absent, negligible changes in color and absorbance were observed, indicating that HMMo-SAzyme indeed possessed peroxidase-like activity. To further explore the catalytic activity of HMMo-SAzyme, Michaelis–Menten steady-state catalytic kinetics were determined. By employing the Michaelis–Menten equation and linear double-reciprocal plots, the Michaelis–Menten constant (K_M) and maximum velocity (V_{max}) for HMMo-SAzyme toward H_2O_2 were determined to be 8.46 mM and 2.66×10^{-7} M/s, respectively (Figure S10). HMMo-SAzyme showed higher catalytic activity compared with other reported SAzymes (Table S1).

To detect the generation of •OH during the reaction that HMMo-SAzyme catalyze H_2O_2, TA was employed as a fluorescent probe. TA itself does not fluoresce; however, upon reaction with •OH, it converts into the highly fluorescent product 2-hydroxyterephthalic acid (TAOH), exhibiting a characteristic fluorescence signal at 435 nm.[49,50] Hence, the fluorescence of TAOH indirectly reflects the amount of •OH generated. When both HMMo-SAzyme and H_2O_2 were present, a strong fluorescence signal was detected (Figure 2B).

Owing to its peroxidase-like activity, HMMo-SAzyme holds potential for antibacterial applications. However, akin to many previously reported peroxidase-like nanozymes, the catalytic activity of HMMo-SAzyme was influenced by temperature (Figure S11) and pH (Figure 2C). Particularly, under near-neutral conditions, HMMo-SAzyme exhibited diminished catalytic activity, which substantially limits its application in bacterial infection microenvironments. To address this, we investigated the effect of GOx catalyzing the conversion of glucose to gluconic acid for pH reduction. When glucose and GOx coexisted, the pH of the system significantly decreased from 7.2 to 3.9 (Figure S12A). Moreover, the pH decreased gradually with increasing glucose concentration (Figure S12B). The use of methyl red as a pH indicator
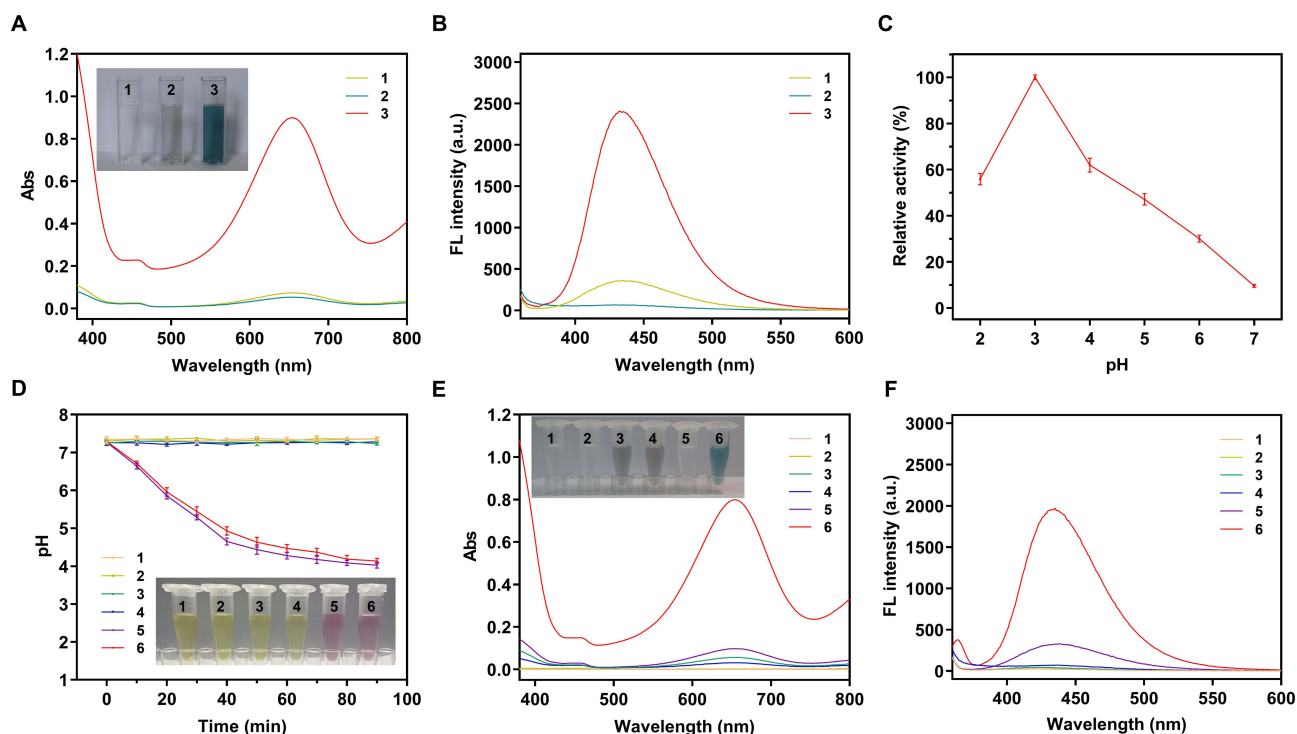

Figure 2 (**A**) UV–vis spectra and photographs of different reaction systems: (1) H_2O_2 + TMB, (2) HMMo-SAzyme + TMB, and (3) HMMo-SAzyme + H_2O_2 + TMB. (**B**) Fluorescence spectra of different reaction systems: (1) H_2O_2 + TA, (2) HMMo-SAzyme + TA, and (3) HMMo-SAzyme + H_2O_2 + TA. (**C**) Peroxidase-like activity of HMMo-SAzyme at different pH values. Data are shown as mean ± SD. (**D**) pH value versus reaction time under different reaction systems; insets are the corresponding photographs in the presence of methyl red. Data are shown as mean ± SD. (**E**) UV–vis spectra and photographs of different reaction systems in the presence of TMB. (**F**) Fluorescence spectra of different reaction systems in the presence of TA. Different reaction systems in (**D–F**): (1) PBS, (2) glucose, (3) HMMo/GOx, (4) glucose + HMMo-SAzyme, (5) glucose + GOx, (6) glucose + HMMo/GOx.

more explicitly demonstrated the pH changes in the solution (Figure S12C and D). These findings confirm that GOx-catalyzed decomposition of glucose can effectively reduce the pH of the system.

The cascade catalytic performance of HMMo/GOx was further investigated through different reaction setups, and the pH changes in each reaction system were monitored using a pH meter and methyl red. The results revealed a significant decrease in pH when glucose and HMMo/GOx coexisted, with the reduction nearly equivalent to that when the same concentrations of glucose and GOx were used (Figure 2D). This indicated that GOx within HMMo/GOx retained robust catalytic activity. When TMB was added to each reaction system, group (6) exhibited a distinct blue color and strong characteristic absorption at 652 nm, whereas control groups (1)–(5) showed negligible changes in color and absorbance (Figure 2E). These findings indicated that the catalytic cascade reaction of HMMo/GOx could proceed smoothly in the presence of glucose as a substrate. Furthermore, the generation of •OH in each group was analyzed by adding TA (Figure 2F); a substantial amount of •OH was generated in group (6), whereas only negligible fluorescence signals were observed in groups (1)–(5). ESR spectra showed characteristic peaks, with an intensity ratio of 1:2:2:1, in group (6), whereas negligible ESR signals were obtained in groups (1)–(5) (Figure S13). These results confirm that HMMo/GOx could efficiently generate •OH through a catalytic cascade reaction utilizing glucose as a substrate.

To mitigate damage to normal cells and tissues caused by •OH generated in the cascade catalytic reaction, HA was used to encapsulate HMMo/GOx. The activation of HMMo/GOx@HA was studied in PBS to simulate the physiological microenvironment of infection. The results showed that the pH of the HMMo/GOx@HA group without HAase treatment only decreased to 6.4 (Figure S14A), and no significant changes in color or absorbance were observed after the addition of TMB (Figure S14B). However, upon HAase treatment, the changes in the HMMo/GOx@HA group were similar to those in the HMMo/GOx group, suggesting that HMMo/GOx@HA could be activated by HAase to initiate the cascade catalytic reaction.

In vitro Antibacterial Activity of the HMMo/GOx@HA Nanoreactor

Given the capability of HMMo/GOx@HA to convert glucose into •OH, we proceeded to investigate its antibacterial activity against both gram-positive *S. aureus* and gram-negative *E. coli*. Initially, we examined the effects of glucose and HMMo/GOx@HA concentrations on the antibacterial performance. The survival rates of both *S. aureus* and *E. coli* were <10% when the concentrations of glucose and HMMo/GOx@HA were 15 mM and 100 µg/mL, respectively (Figures S15 and S16). These results demonstrated that HMMo/GOx@HA exhibited high antibacterial activity in the presence of glucose, and its antibacterial effect was directly dependent on glucose and HMMo/GOx@HA concentrations.

The antibacterial mechanism of HMMo/GOx@HA was further explored by subjecting the bacteria to different treatments. As depicted in Figure 3A and B, the survival rates of bacteria in groups (2)–(4) remained essentially unchanged compared with that in group (1), indicating that the antibacterial activity of glucose, HMMo/GOx@HA, or glucose + HMMo-SAzyme was negligible. Following treatment with group (5), the survival rates of *S. aureus* and *E. coli* were 64.77% and 70.26%, respectively. This insufficient antibacterial effect can be attributed to the production of H_2O_2, which could only partially kill the bacteria. In contrast, the survival rates of *S. aureus* and *E. coli* in group (6) were significantly lower, being 5.41% and 8.32%, respectively. The enhanced antibacterial performance in this group was attributed to the occurrence of the cascade catalytic reaction, wherein H_2O_2 produced by the oxidation of glucose was further catalyzed to generate •OH, which possesses stronger antibacterial activity. This cascade catalytic reaction effectively amplified the bactericidal effect, rendering HMMo/GOx@HA a highly effective antibacterial agent.

The results of live/dead bacterial staining experiments showed that both *S. aureus* and *E. coli* in groups (1)–(4) displayed strong green fluorescence and minimal red fluorescence (Figure 3C), indicating that the majority of bacteria survived. Group (5) exhibited partial red fluorescence, indicating that H_2O_2 produced by glucose oxidation failed to effectively kill the bacteria. However, in group (6), intense red fluorescence was observed, indicating a significant increase in the number of bacterial deaths. These findings were consistent with the colony counts, providing further evidence that HMMo/GOx@HA displayed superior antibacterial properties in the presence of glucose.

The morphological changes in bacteria under different treatment conditions were observed using SEM (Figure 3D). After (1) PBS treatment, *S. aureus* exhibited a smooth surface, normal morphology, and intact cell membranes. Similarly, after (2) glucose, (3) HMMo/GOx@HA, and (4) glucose + HMMo-SAzyme treatments, almost negligible damage was
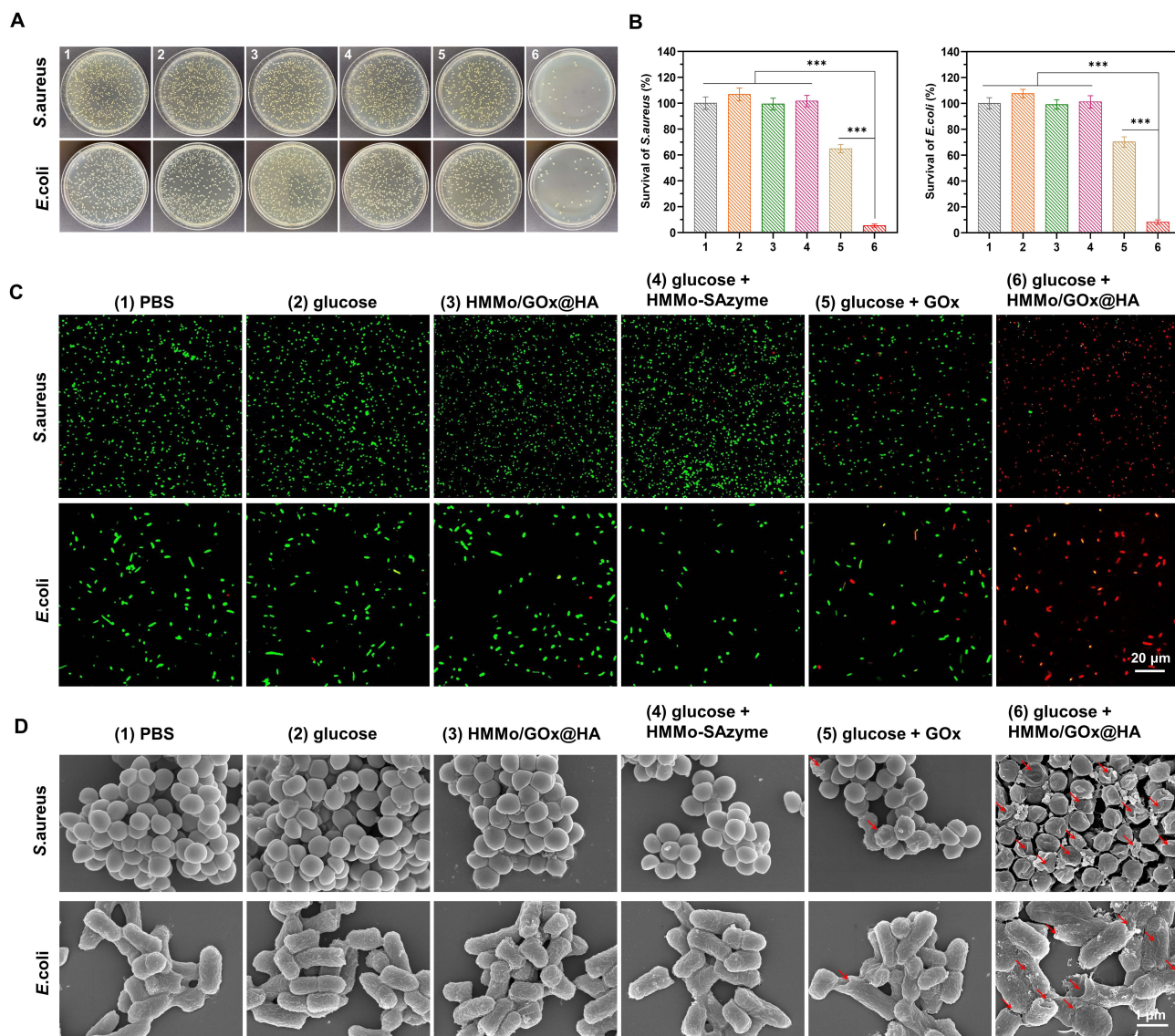
Figure 3 (**A**) Photographs of bacterial colonies formed by *S. aureus* and *E. coli*. (**B**) Relative bacterial survival of *S. aureus* and *E. coli*. Data are shown as mean ± SD, ***P < 0.001. (**C**) CLSM images for live/dead bacterial staining assay of *S. aureus* and *E. coli*. (**D**) SEM images of *S. aureus* and *E. coli*. Red arrows indicate the location of bacterial rupture. *S. aureus* and *E. coli* in (**A–D**) treated with (1) PBS, (2) glucose, (3) HMMo/GOx@HA, (4) glucose + HMMo-SAzyme, (5) glucose + GOx, and (6) glucose + HMMo/GOx@HA.

observed in *S. aureus*, indicating minimal antibacterial effect on *S. aureus*. In group (5), the surfaces of *S. aureus* showed only partial wrinkling, suggesting that H_2O_2 had weak antibacterial activity against *S. aureus*. However, in group (6), following glucose + HMMo/GOx@HA treatment, the cell walls of *S. aureus* displayed severe damage and the cell surface displayed irregularly shaped holes, signifying that *S. aureus* was subjected to severe oxidative damage by •OH produced through the catalytic cascade reaction. The integrity of the bacterial cell membrane system was disrupted, and the bacterial contents leaked, resulting in the death of bacteria. Similar morphological changes were observed for *E. coli*. DCFH-DA probe was used to detect ROS in bacteria. When the bacteria were incubated with glucose + HMMo/GOx@HA, green fluorescence was observed, whereas almost no fluorescence was emitted in the control group (Figure S17), which further suggested that the death of bacteria was caused by ROS produced by the cascade catalysis of the nanosystem.

Furthermore, under the same concentrations of H_2O_2 and glucose, the antibacterial performance of the glucose + HMMo/GOx@HA group was notably superior to that of the H_2O_2 + HMMo-SAzyme group (Figure S18). These results

clearly demonstrated that gluconic acid, generated from glucose oxidation, can significantly enhance the catalytic activity of HMMo-SAzyme, thereby, promoting the production of •OH.

In vivo Bacterial Infection Treated with the HMMo/GOx@HA Nanoreactor

Bacterial infection models were established on the back of BALB/c mice. After successful modeling, the mice were randomly divided into six groups and subjected to different treatments. Compared with the control group, the wound area treated with glucose + HMMo/GOx@HA showed a significant reduction and was almost completely healed by the 7th day of treatment, with the appearance of new pink skin (Figure 4A and B). This indicated that •OH produced by the
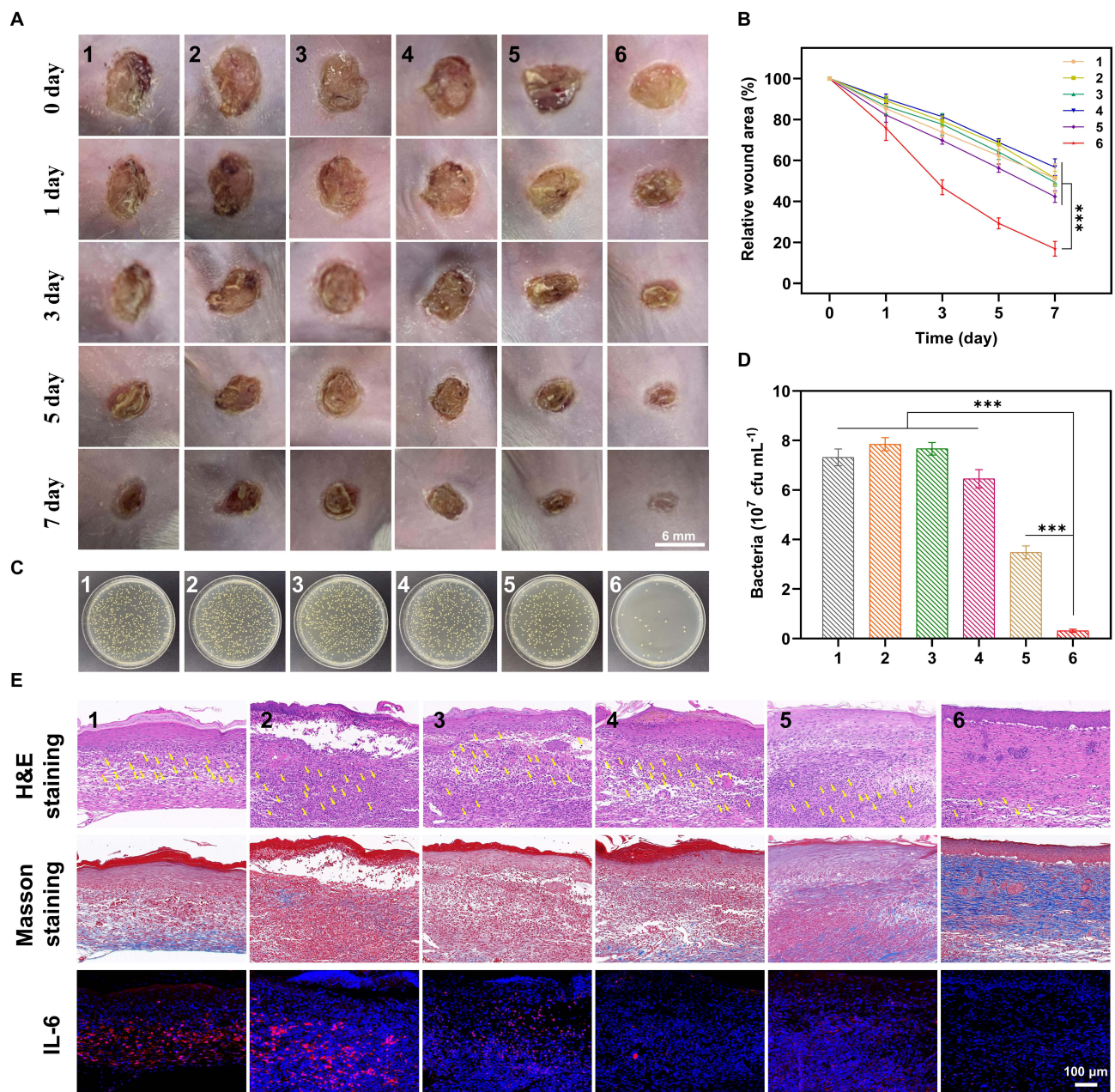

Figure 4 (**A**) Photographs of wounds of mice infected with *S. aureus* after receiving different treatments. (**B**) Relative wound area of mice. Data are shown as mean ± SD, ***P < 0.001. (**C**) Photographs of bacterial colonies formed by bacteria obtained from wound tissues. (**D**) Number of surviving bacteria in the infected wounds of mice with different treatments. Data are shown as mean ± SD, ***P < 0.001. (**E**) H&E staining, Masson staining, and immunofluorescence staining for IL-6 of wounds after 7 days of treatment. Yellow arrows indicate the infiltration of inflammatory cells. Different treatments in (**A**–**E**): (1) PBS, (2) glucose, (3) HMMo/GOx@HA, (4) glucose + HMMo-SAzyme, (5) glucose + GOx, (6) glucose + HMMo/GOx@HA.

catalytic cascade reaction in group (6) effectively inhibited bacterial infection and promoted wound healing. The antibacterial effect was further evaluated by determining the number of bacteria on the wounds using the plate colony counting method (Figure 4C and D). The results revealed that the bacterial survival rate in group (6) decreased significantly to 4.28%, which was significantly lower than that in the other treatment groups, consistent with the results of the wound healing experiment.

To assess wound healing at the tissue level, H&E and Masson staining were performed on the wound tissue sections. With H&E staining, a large number of inflammatory cells and incomplete epidermal structures were observed in groups (1)–(5), whereas in group (6), inflammatory cells were significantly reduced, a relatively complete epidermal structure was evident, and the thickness of the dermal increased.(Figures 4E and S19A). With Masson staining, group (6) exhibited the highest collagen fiber (blue) formation compared with that in the other groups (Figures 4E and S19B). Additionally, the levels of interleukin 6 (IL-6), a typical inflammatory cytokine, were examined in the wound tissue to assess inflammation. IL-6 levels were significantly lower after treatment with glucose + HMMo/GOx@HA compared with that in the other groups (Figures 4E and S19C), indicating a milder inflammatory response around the wounds. Overall, these results showed that the designed HMMo/GOx@HA nanoreactor, in the presence of glucose, exhibited excellent antibacterial activity and effectively promoted wound healing in vivo.

Biosafety of the HMMo/GOx@HA Nanoreactor

As a potential antibacterial agent, the HMMo/GOx@HA nanoreactor was assessed for its biosafety. First, a hemolysis assay was performed. Generally, a hemolysis rate of less than 5% indicates that no hemolysis is observed. Compared with the control group, hemolysis was not observed even when the concentration of HMMo/GOx@HA was as high as 500 µg/mL (Figure 5A), indicating excellent hemocompatibility of HMMo/GOx@HA. Next, the in vitro cytotoxicity of HMMo/
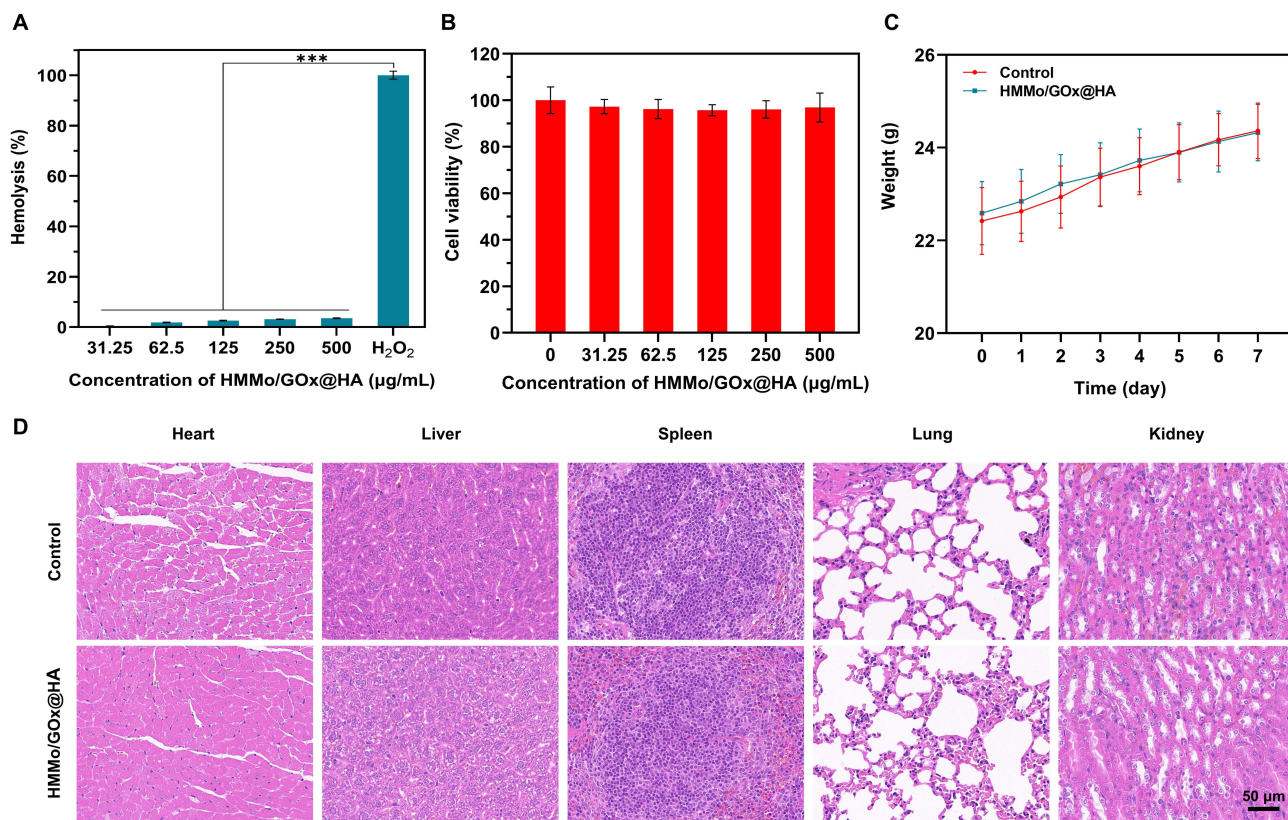

Figure 5 (**A**) Relative hemolysis ratio of red blood cells after treatment with different concentrations of HMMo/GOx@HA. Data are shown as mean ± SD, ***P < 0.001. (**B**) Cell viability of HUVECs after incubation with HMMo/GOx@HA at various concentrations for 24 h. Data are shown as mean ± SD. (**C**) Changes in body weight of healthy mice following tail vein injection of PBS or HMMo/GOx@HA. Data are shown as mean ± SD. (**D**) H&E staining images of major organs of mice after treatment with PBS or HMMo/GOx@HA.

GOx@HA was investigated using HUVECs. The results demonstrated that HMMo/GOx@HA showed negligible cytotoxicity (Figure 5B). Furthermore, in vivo toxicity was evaluated by injecting HMMo/GOx@HA into the tail vein of BALB/c mice. Over a period of 7 days, no significant changes in body weight were observed (Figure 5C), indicating that HMMo/GOx@HA did not adversely affect the normal development of the mice. Blood biochemical examination revealed no significant differences in the biochemical indices between the HMMo/GOx@HA and control groups (Figure S20), indicating that HMMo/GOx@HA did not cause significant damage to the liver and kidneys in the mice. Additionally, H&E staining of major organs showed that HMMo/GOx@HA did not induce notable inflammation or damage to the heart, lung, spleen, liver, and kidney (Figure 5D). These comprehensive results demonstrate that the HMMo/GOx@HA nanoreactor is a safe and biocompatible antibacterial system, with negligible toxicity both in vitro and in vivo.

Conclusion

In this study, a novel HMMo-SAzyme was synthesized using a controlled chemical etching approach and pyrolysis strategy. Compared with SAzymes reported previously, this unique SAzyme exhibited not only exceptional peroxidase-like activity, but also the capability to act as a carrier for loading macromolecular substances owing to its mesoporous structure and large internal voids. On this basis, a nanoreactor (HMMo/GOx@HA) was constructed by loading GOx into the HMMo-SAzyme and encapsulating it within HA. The designed nanoreactor exhibited a cascade catalytic antibacterial mechanism in vivo. Upon reaching the infected site, the outer HA layer of the nanoreactor could be degraded by HAase, exposing GOx, which continuously converted glucose into gluconic acid. This process significantly enhanced the catalytic activity of HMMo-SAzyme. Moreover, substantial amount of the generated H_2O_2 underwent further conversion to •OH by HMMo-SAzyme, leading to effective antibacterial action. Biological experiments confirmed the excellent antibacterial efficacy and safety of the nanoreactor. The successful construction of a functional hollow mesoporous nanoreactor for antibacterial therapy represents a significant advancement in the field, offering a promising strategy for further developments in biomedical applications of SAzymes.

Abbreviations

CLSM, confocal laser scanning microscope; EDS, energy-dispersive X-ray spectroscopy; GOx, glucose oxidase; HA, hyaluronic acid; HAADF-STEM, high-angle annular dark-field scanning transmission electron microscope; HAase, hyaluronidase; HMMo-SAzyme, hollow mesoporous molybdenum single-atom nanozyme; HMo-ZIF-8, hollow molybdenum-doped zeolitic imidazolate framework; HUVECs, human umbilical vein endothelial cells. ICP-OES, inductively coupled plasma optical emission spectrometry; Mo-ZIF-8, molybdenum-doped zeolitic imidazolate framework; SAzyme, single-atom nanozyme; SEM, scanning electron microscope; TA, terephthalic acid; TEM, transmission electron microscope; TMB, 3,3',5,5'-tetramethylbenzidine; XRD, X-ray diffraction; ZIF-8, zeolitic imidazolate framework-8.

Ethics Approval and Consent to Participate

All experimental procedures on animals were performed in strict accordance with the Guide for the Care and Use of Laboratory Animals, and were approved by the Institutional Animal Care and Use Committee of the Air Force Medical University (approval number: 20230066; approval date: October 8, 2022).

Funding

Disclosure

Prof. Dr. Hong Wu reports a pending patent "The invention relates to a hollow mesoporous single atom molybdenum nanomase, a preparation method and application of nano-enzyme reactor based on it". The authors report no other conflicts of interest in this work.

References

1. Hernando-Amado S, Coque TM, Baquero F, Martínez JL. Defining and combating antibiotic resistance from one health and global health perspectives. *Nat Microbiol*. 2019;4(9):1432–1442. doi:10.1038/s41564-019-0503-9
2. Li X, Bai H, Yang Y, Yoon J, Wang S, Zhang X. Supramolecular antibacterial materials for combatting antibiotic resistance. *Adv Mater*. 2019;31 (5):1805092–1805119. doi:10.1002/adma.201805092
3. Li H, Li D, Chen F, et al. Nanosilver-decorated biodegradable mesoporous organosilica nanoparticles for GSH-responsive gentamicin release and synergistic treatment of antibiotic-resistant bacteria. *Int J Nanomed*. 2021;16:4631–4642. doi:10.2147/IJN.S315067
4. Tong C, Zhong X, Yang Y, et al. PB@PDA@Ag nanosystem for synergistically eradicating MRSA and accelerating diabetic wound healing assisted with laser irradiation. *Biomaterials*. 2020;243:119936–119949. doi:10.1016/j.biomaterials.2020.119936
5. Wei H, Gao L, Fan K, et al. Nanozymes: a clear definition with fuzzy edges. *Nano Today*. 2021;40:101269–101274. doi:10.1016/j.nantod.2021.101269
6. Zhang R, Bai X, Tao Y, et al. Edge-site engineering of defective $Fe-N_4$ nanozymes with boosted catalase-like performance for retinal vasculopathies. *Adv Mater*. 2022;34(39):2205324. doi:10.1002/adma.202205324
7. Yang J, Zhang R, Zhao H, et al. Bioinspired copper single-atom nanozyme as a superoxide dismutase-like antioxidant for sepsis treatment. *Exploration*. 2022;2(4):20210267–20210276. doi:10.1002/EXP.20210267
8. Ou H, Qian Y, Yuan L, et al. Spatial position regulation of Cu single atom site realizes efficient nanozyme photocatalytic bactericidal activity. *Adv Mater*. 2023;35(46):2305077–2305086. doi:10.1002/adma.202305077
9. Liu X, Liu Q, He X, et al. NIR-II-enhanced single-atom-nanozyme for sustainable accelerating bacteria-infected wound healing. *Appl Surf Sci* 2023;612:155866–155873. doi:10.1016/j.apsusc.2022.155866
10. Feng Y, Qin J, Zhou Y, Yue Q, Wei J. Spherical mesoporous Fe-N-C single-atom nanozyme for photothermal and catalytic synergistic antibacterial therapy. *J Colloid Interface Sci*. 2022;606:826–836. doi:10.1016/j.jcis.2021.08.054
11. Zhu J, Li Q, Li X, Wu X, Yuan T, Yang Y. Simulated enzyme activity and efficient antibacterial activity of copper-doped single-atom nanozymes. *Langmuir*. 2022;38(22):6860–6870. doi:10.1021/acs.langmuir.2c00155
12. Wang X, Shi Q, Zha Z, et al. Copper single-atom catalysts with photothermal performance and enhanced nanozyme activity for bacteria-infected wound therapy. *Bioact Mater*. 2021;6(12):4389–4401. doi:10.1016/j.bioactmat.2021.04.024
13. Vatansever F, de Melo WC, Avci P, et al. Antimicrobial strategies centered around reactive oxygen species-bactericidal antibiotics, photodynamic therapy, and beyond. *FEMS Microbiol Rev*. 2013;37(6):955–989. doi:10.1111/1574-6976.12026
14. Xu B, Wang H, Wang W, et al. A single-atom nanozyme for wound disinfection applications. *Angew Chem Int Ed Engl*. 2019;58(15):4911–4916. doi:10.1002/anie.201813994
15. Huo M, Wang L, Zhang H, Zhang L, Chen Y, Shi J. Construction of single-iron-atom nanocatalysts for highly efficient catalytic antibiotics. *Small*. 2019;15(31):1901834–1901843. doi:10.1002/smll.201901834
16. Natalio F, André R, Hartog AF, et al. Vanadium pentoxide nanoparticles mimic vanadium haloperoxidases and thwart biofilm formation. *Nat Nanotechnol*. 2012;7(8):530–535. doi:10.1038/nnano.2012.91
17. Wang X, Meier RJ, Wolfbeis OS. Fluorescent pH-sensitive nanoparticles in an agarose matrix for imaging of bacterial growth and metabolism. *Angew Chem Int Ed Engl*. 2013;52(1):406–409. doi:10.1002/anie.201205715
18. Liu X, Yan Z, Zhang Y, et al. Two-dimensional metal–organic framework/enzyme hybrid nanocatalyst as a benign and self-activated cascade reagent for in vivo wound healing. *ACS Nano*. 2019;13(5):5222–5230. doi:10.1021/acsnano.8b09501
19. Wang X, Fan L, Cheng L, et al. Biodegradable nickel disulfide nanozymes with GSH-depleting function for high-efficiency photothermal-catalytic antibacterial therapy. *iScience*. 2020;23(7):101281–101298. doi:10.1016/j.isci.2020.101281
20. Gao L, Giglio KM, Nelson JL, Sondermann H, Travis AJ. Ferromagnetic nanoparticles with peroxidase-like activity enhance the cleavage of biological macromolecules for biofilm elimination. *Nanoscale*. 2014;6(5):2588–2593. doi:10.1039/C3NR05422E
21. Dickinson BC, Chang CJ. chemistry and biology of reactive oxygen species in signaling or stress responses. *Nat Chem Biol*. 2011;7(8):504–511. doi:10.1038/nchembio.607
22. Li C, Sun Y, Li X, et al. Bactericidal effects and accelerated wound healing using Tb_4O_7 nanoparticles with intrinsic oxidase-like activity. *J Nanobiotechnol*. 2019;17(1):54–63. doi:10.1186/s12951-019-0487-x
23. Sun K, Tang Y, Li Q, et al. In vivo dynamic monitoring of small molecules with implantable polymer-dot transducer. *ACS Nano*. 2016;10 (7):6769–6781. doi:10.1021/acsnano.6b02386
24. Huo M, Wang L, Chen Y, Shi J. Tumor-selective catalytic nanomedicine by nanocatalyst delivery. *Nat Commun*. 2017;8(1):357–368. doi:10.1038/s41467-017-00424-8
25. Chang K, Liu Z, Fang X, et al. Enhanced phototherapy by nanoparticle-enzyme via generation and photolysis of hydrogen peroxide. *Nano Lett*. 2017;17(7):4323–4329. doi:10.1021/acs.nanolett.7b01382
26. Li S, Cheng H, Xie B, et al. Cancer cell membrane camouflaged cascade bioreactor for cancer targeted starvation and photodynamic therapy. *ACS Nano*. 2017;11(7):7006–7018. doi:10.1021/acsnano.7b02533
27. Zhu W, Chen Z, Pan Y, et al. Functionalization of hollow nanomaterials for catalytic applications: nanoreactor construction. *Adv Mater*. 2018;31 (38):1800426–1800455. doi:10.1002/adma.201800426
28. Yin Y, Rioux RM, Erdonmez CK, Hughes S, Somorjai GA, Alivisatos AP. Formation of hollow nanocrystals through the nanoscale Kirkendall effect. *Science*. 2004;304(5671):711–714. doi:10.1126/science.1096566
29. Fodor D, Ishikawa T, Krumeich F, van Bokhoven JA. Synthesis of single crystal nanoreactor materials with multiple catalytic functions by incipient wetness impregnation and ion exchange. *Adv Mater*. 2015;27(11):1919–1923. doi:10.1002/adma.201404628
30. Qiu P, Ma B, Hung CT, Li W, Zhao D. Spherical mesoporous materials from single to multilevel architectures. *Acc Chem Res*. 2019;52 (10):2928–2938. doi:10.1021/acs.accounts.9b00357
31. Wang G, Yang S, Cao L, et al. Engineering mesoporous semiconducting metal oxides from metal-organic frameworks for gas sensing. *Coord Chem Rev*. 2021;445:214086–214106. doi:10.1016/j.ccr.2021.214086
32. Wei J, Sun Z, Luo W, et al. New insight into the synthesis of large-pore ordered mesoporous materials. *J Am Chem Soc*. 2017;139(5):1706–1713. doi:10.1021/jacs.6b11411

33. Wang Z, Wang H, Zhang Z, et al. Synthesis of Pd nanoframes by excavating solid nanocrystals for enhanced catalytic properties. *ACS Nano*. 2016;11(1):163–170. doi:10.1021/acsnano.6b06491

34. Gao S, Lin H, Zhang H, Yao H, Chen Y, Shi J. Nanocatalytic tumor therapy by biomimetic dual inorganic nanozyme-catalyzed cascade reaction. *Adv Sci*. 2018;6(3):1801733–1801744. doi:10.1002/advs.201801733

35. Wei X, Zheng D, Zhao M, et al. Cross-linked polyphosphazene hollow nanosphere-derived N/P-doped porous carbon with single nonprecious metal atoms for the oxygen reduction reaction. *Angew Chem Int Ed Engl*. 2020;59(34):14639–14646. doi:10.1002/anie.202006175

36. Novotny JA, Peterson CA. Molybdenum. *Adv Nutr*. 2018;9(3):272–273. doi:10.1093/advances/nmx001

37. Zhang Y, Li D, Tan J, et al. Near-infrared regulated nanozymatic / photothermal / photodynamic triple-therapy for combating multidrug-resistant bacterial infections via oxygen-vacancy molybdenum trioxide nanodots. *Small*. 2021;17(1):2005739–2005750. doi:10.1002/smll.202005739

38. Li Y, Fu R, Duan Z, Zhu C, Fan D. Construction of multifunctional hydrogel based on the tannic acid-metal coating decorated MoS$_2$ dual nanozyme for bacteria-infected wound healing. *Bioact Mater*. 2022;9:461–474. doi:10.1016/j.bioactmat.2021.07.023

39. Wang T, Zhang X, Mei L, et al. Two-step gas/liquid strategy for production of N-doped defect-rich transition metal dichalcogenide nanosheets and their antibacterial applications. *Nanoscale*. 2020;12(15):8415–8424. doi:10.1039/D0NR00192A

40. Ye W, Chen S, Lin Y, et al. Precisely tuning the number of fe atoms in clusters on N-doped carbon toward acidic oxygen reduction reaction. *Chem*. 2019;5(11):2865–2878. doi:10.1016/j.chempr.2019.07.020

41. Yang M, Xu W, Chen Z, et al. Engineering hibiscus-like riboflavin/ZIF-8 microsphere composites to enhance transepithelial corneal cross-linking. *Adv Mater*. 2022;34(21):2109865–2109881. doi:10.1002/adma.202109865

42. Liu W, Huang J, Yang Q, et al. Multi-shelled hollow metal-organic frameworks. *Angew Chem Int Ed Engl*. 2017;56(20):5512–5516. doi:10.1002/anie.201701604

43. Hu M, Ju Y, Liang K, Suma T, Cui J, Caruso F. Void Engineering in metal-organic frameworks via synergistic etching and surface functionalization. *Adv Funct Mater*. 2016;26(32):5827–5834. doi:10.1002/adfm.201601193

44. Xiong Y, Dong J, Huang ZQ, et al. Single-atom Rh/N-doped carbon electrocatalyst for formic acid oxidation. *Nat Nanotechnol*. 2020;15(5):390–397. doi:10.1038/s41565-020-0665-x

45. Li Z, Chen Y, Ji S, et al. Iridium single-atom catalyst on nitrogen-doped carbon for formic acid oxidation synthesized using a general host-guest strategy. *Nat Chem*. 2020;12(8):764–772. doi:10.1038/s41557-020-0473-9

46. Wang X, Chen Z, Zhao X, et al. Regulation of coordination number over single co sites: triggering the efficient electroreduction of CO$_2$. *Angew Chem Int Ed Engl*. 2018;57(7):1944–1948. doi:10.1002/anie.201712451

47. Zhang L, Jia Y, Gao G, et al. Graphene defects trap atomic Ni species for hydrogen and oxygen evolution reactions. *Chem*. 2018;4(2):285–297. doi:10.1016/j.chempr.2017.12.005

48. Chen W, Pei J, He CT, et al. Rational design of single molybdenum atoms anchored on N-doped carbon for effective hydrogen evolution reaction. *Angew Chem Int Ed Engl*. 2017;56(50):16086–16090. doi:10.1002/anie.201710599

49. Liu Z, Wang F, Ren J, Qu X. A series of MOF/Ce-based nanozymes with dual enzyme-like activity disrupting biofilms and hindering recolonization of bacteria. *Biomaterials*. 2019;208:21–31. doi:10.1016/j.biomaterials.2019.04.007

50. Wang Z, Dong K, Liu Z, et al. Activation of biologically relevant levels of reactive oxygen species by Au/g-C$_3$N$_4$ hybrid nanozyme for bacteria killing and wound disinfection. *Biomaterials*. 2017;113:145–157. doi:10.1016/j.biomaterials.2016.10.041